Research Square

Preprints are preliminary reports that have not undergone peer review.
They should not be considered conclusive, used to inform clinical practice,
or referenced by the media as validated information.

Research on the Material Removal Mechanism and Experiments of Electrolytic Plasma Polishing for High-Strength Steel

Pengfei Li
Feng Yang
yfwfy08170163.com

Shenyang ligong University https://orcid.org/0000-0003-1581-5395
Bingxin Liu
Xiankun Cheng

Research Article

Keywords: High-strength steel, Electrolyte Plasma Polishing, Surface roughness

Posted Date: July 2nd, 2026

DOI: https://doi.org/10.21203/rs.3.rs-8392619/v1

License: This work is licensed under a Creative Commons Attribution 4.0 International License.
Read Full License

Research on the Material Removal Mechanism and Experiments of Electrolytic Plasma Polishing for High-Strength Steel

Pengfei Li[a], Feng Yang[a*], Bingxin Liu[b] and Xiankun Cheng[a]

[a] School of Equipment Engineering, Shenyang Ligong University, Shenyang, 110159, People's Republic of China.

[b] Qiqihar Heping Heavy Industries Group Co., LTD. of CNIGCL. Qiqihar, 161000, People's Republic of China.

Abstract

This study aims to reduce the surface roughness of high-strength steel to meet the stringent requirements for high surface quality in engineering applications. To achieve this, the electrolyte plasma polishing (EPP) technology is proposed for precision machining of its surface. Centering on the material removal mechanism of EPP, a systematic investigation is carried out by integrating multi-physics field modeling and simulation with experimental validation. The paper elucidates the fundamental principles and material removal mechanism of electrolyte plasma polishing. It establishes mathematical models for the electric and flow fields, gas-liquid two-phase flow, and the process characterizing "peak removal". Dynamic simulation analysis is conducted on key physical phenomena during polishing, focusing on simulating the formation and evolution of the gaseous insulating layer on the anode surface and the "peak removal" behavior reflecting the surface leveling process. Research shows that the "peak removal" process is initiated by electrochemical dissolution at the workpiece surface along with the associated bubble evolution and collapse. The material removal mechanism is ascribed to the combined action of fluid erosion, formation of local discharge channels, and discharge at the tips of surface asperities. A series of polishing experiments was conducted, enabling systematic characterization of the specimens' surface roughness, microscopic morphology, 3D topography, elemental composition,

and microhardness both pre- and post-polishing. The results indicate that the polishing treatment significantly enhances surface smoothness, imparting a metallic luster, substantially reduces surface roughness, and leads to a marked improvement in surface morphology. A significant decrease in surface oxygen content, a slight increase in chromium content, and a minor reduction in microhardness were observed. This research deepens the mechanistic understanding of the Electrolyte Plasma Polishing process, thereby furnishing a theoretical foundation and experimental data to support its optimization and precise control.

Keywords: High-strength steel; Electrolyte Plasma Polishing; Surface roughness;

1 Introduction

As the core key component of the artillery fire system, the processing quality of its internal rifling directly determines the projectile's directivity, initial motion state, and the gun's firing accuracy, range and service life [1-4]. As the body tube is generally made of special performance alloy steel with high strength, high hardness and high abrasion resistance, and the rifling itself is a kind of large depth-to-diameter ratio, heteromorphic cross-section of the deep bore silhouette structure, resulting in the machining of the surface quality is difficult to ensure that there are often microscopic unevenness, residual stress and surface defects and other problems [5,6].

At present, mechanical polishing remains the predominant process for artillery barrel rifling in China, primarily involving traditional methods such as honing and manual brushing with lead laps. While capable of reducing surface roughness to a certain degree, these techniques are inherently limited by low efficiency, high labor intensity, and poor processing uniformity [7]. Particularly in geometrically complex regions like the rifling groove bottoms and land edges, conventional polishing tools are inadequate for achieving uniform and effective surface finishing, which critically compromises the homogeneity and stability of the barrel's performance. Furthermore, the metal dust produced during mechanical polishing operations presents significant health risks to personnel [8]. Although chemical polishing can adapt to complex geometries, the strong acidic media commonly used can easily cause environmental pollution, incur high waste liquid treatment costs, and the achievable surface roughness range (typically 0.5–10 μm) struggles to meet the requirements for high-precision barrels [9]. Consequently, there is a pressing industrial demand to develop an environmentally friendly and highly efficient polishing technique suitable for complex profiles, which is crucial for advancing barrel manufacturing quality and ensuring weapon system reliability.

In this context, electrolyte plasma polishing (EPP) has garnered considerable interest as a novel non-contact finishing technique, owing to its distinct benefits for surface processing of components with intricate geometries. The process relies on

applying a high voltage within a dilute neutral salt electrolyte to generate a vapor sheath and plasma discharge, which enables material removal and surface smoothening via preferential removal of microscopic surface peaks [10-12]. In contrast to traditional techniques, EPP presents benefits including absence of tool wear, high adaptability, environmental compatibility, and elevated processing efficiency, rendering it especially apt for the precision polishing of parts with deep-hole and complex internal cavity structures, such as gun barrels [13-16].

In recent years, scholars both domestically and internationally have conducted fruitful explorations regarding the theory and process of electrolyte plasma polishing. Wang et al. [8,17,18] studied the underlying mechanism of EPP on metallic surfaces, developed a model demonstrating a proportional relationship between material removal rate and current density, and highlighted electrolyte temperature, concentration, and immersion depth as key process parameters. Through orthogonal experiments, Yuan et al. [19] optimized the EPP parameters for selective laser melted 316L stainless steel, achieving a notable reduction in surface roughness from 2.108 μm to 0.213 μm, alongside an increase in surface chromium content and improved corrosion resistance. Zai et al. [20] optimized the EPP parameters for TC4 titanium alloy, successfully lowering the surface roughness from 0.368 μm to 0.024 μm under conditions of 400 s, 90 °C, and 300 V, thereby offering an environmentally friendly process alternative for precision machining of high-strength alloys. Dai et al. [21] applied an environmentally benign EPP process to 316L stainless steel ornaments. Through regulation of the initial electrolyte temperature, pre-polishing sandpaper grit, and an estimated polishing time of 0.37 min/cm², they successfully diminished surface roughness and markedly improved luminosity, accomplishing a high-quality mirror-finish polish on the ornamental surfaces. Liu et al. [22] studied the influence of plasma electrolytic polishing (PEP) on the surface topography and corrosion resistance of SLM-produced TC4 titanium alloy components. Their findings demonstrated that PEP effectively removed the characteristic surface imperfections from the SLM process, resulting in a more uniform and smoother finish that exhibited superior corrosion resistance. Regarding specialized barrel machining, Ge [23] investigated the electrochemical

machining of rifling for thin-walled aluminum alloy barrels, attaining a surface roughness of Ra 0.741 μm alongside a dimensional accuracy of 0.035 mm. Innovative approaches introduced by Xue et al. [24], including the forced helical flow method, high-pressure water jet circulation method, and magnetorheological fluid-based techniques, have also offered fresh perspectives for tackling the difficulties in processing barrel rifling grooves and lands.

Despite the proven effectiveness of electrolyte plasma polishing in areas like aerospace and medical device manufacturing, its application to polishing high-strength steel gun barrel rifling is still nascent. Significant gaps exist in systematic research, particularly concerning the control of uniform plasma distribution within deep holes featuring large aspect ratios and non-circular cross-sections, the modulation of electrochemical responses in high-strength steels, and the establishment of correlations between process parameters and resultant surface quality. Consequently, this work proposes employing electrolyte plasma polishing to improve the surface quality of artillery barrel rifling. A systematic study on the material removal mechanism of this technique applied to barrel-grade high-strength steel is conducted. The feasibility and efficacy of the process for finishing the interior of deep-hole components with large aspect-ratio and complex cross-sections are evaluated by comparative analysis of surface roughness, micro-morphology, three-dimensional topography, compositional changes, and microhardness of specimens before and after polishing. This study possesses considerable theoretical merit and practical engineering significance for pioneering new rifling polishing methodologies and advancing the comprehensive performance of gun systems.

2.1 Material removal mechanism

2.1 Fundamentals of electrolyte plasma polishing

As illustrated in Fig. 1, the principle of electrolyte plasma polishing involves using the workpiece 1 as the anode, with the polishing electrolyte 3 and the processing tank 4 jointly serving as the cathode. When a voltage between 250 and 400 V is applied, a coherent vapor layer 2 instantly forms on the workpiece 1 surface, effectively isolating it from the surrounding electrolyte 3. Upon electrical breakdown of this vapor layer, discharge channels are preferentially established at surface micro-peaks, resulting in their selective removal and consequently producing a smoothing and polishing effect.

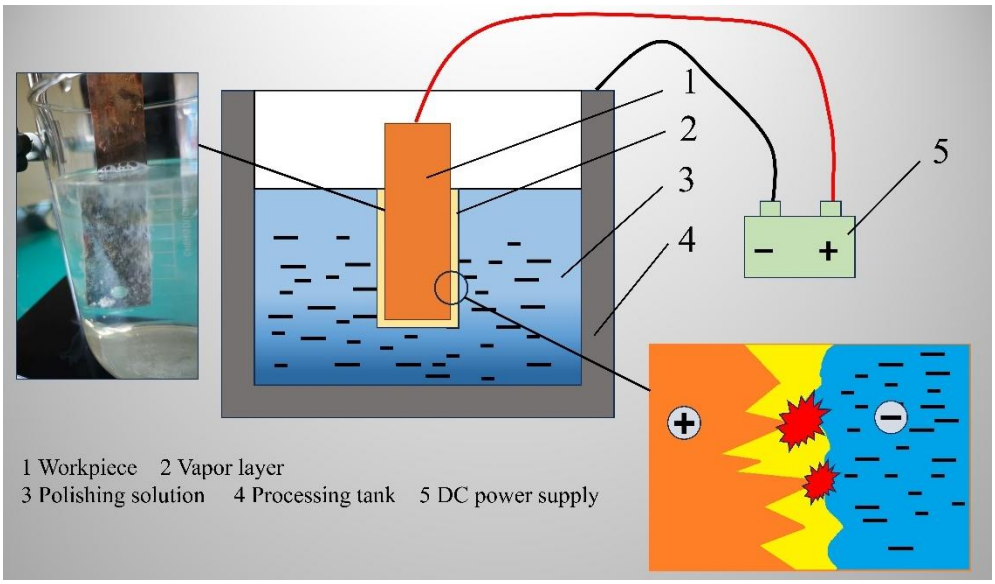


Fig. 1 Schematic diagram of the electrolyte plasma polishing principle

During operation, the workpiece is initially immersed in the polishing solution maintained at a specified temperature and concentration. Upon power application, electrolysis of the electrolyte occurs concurrently with a momentary short circuit resulting from direct workpiece-electrolyte contact, producing intense Joule heating. This rapidly vaporizes the liquid film near the workpiece surface, establishing a stable vapor sheath predominantly consisting of superheated steam. This gaseous envelope markedly elevates the electrical resistance across the anode-cathode gap, causing a localized voltage surge that eventually triggers ionization and breakdown of the vapor sheath, establishing plasma discharge channels. A vigorous and complex physico-

chemical interaction occurs between the plasma and the metal surface: chemical reaction products are generated on the surface, while the discharge activity simultaneously etches them away. A net removal of material from the metal surface is achieved when the etching rate surpasses the formation rate, resulting in a polishing effect evidenced by increased surface brightness and diminished roughness.

2.2 Material removal mechanism in electrolyte plasma polishing

Throughout the electrolyte plasma polishing operation, with a gradual increase in the inter-electrode voltage, the evolution of bubbles surrounding the anode workpiece is observable, encompassing their nucleation, enrichment, and eventual coalescence into a continuous vapor insulation layer. This progression corresponds to three separate phases within the polishing process.

(1) Electrochemical corrosion — Bubble formation

In the absence of an externally applied voltage and with ammonium sulfate solution used as the electrolytic medium, the system is in a state of static equilibrium. Under these conditions, ammonium sulfate dissociates in the aqueous solution into SO_4^{2-}, NH_4^+, H^+ and OH^- ions, as shown in Fig. 2-a. Thus, the main molecular and ionic species existing in the polishing solution are H_2O, SO_4^{2-}, NH_4^+, H^+ and OH^-. This dissociation process is described by the following equation:

$$H_2O \rightarrow H^+ + OH^-$$

$$(NH_4)_2SO_4 \rightarrow 2NH_4^+ + SO_4^{2-}$$

After applying an external electric field, under its influence, H^+ ions become enriched near the cathode region, leading to hydrogen evolution. Simultaneously, OH^- ions accumulate around the anodic workpiece, which subsequently triggers the oxygen evolution reaction. The specific process is illustrated in Fig. 2-b.

The following electrochemical reaction takes place at the anode interface:

$$Fe - 2e^- \rightarrow Fe^{2+}$$

$$Fe - 3e^- \rightarrow Fe^{3+}$$

$$4OH^- - 4e^- \rightarrow O_2 + 2H_2O$$

Conversely, at the cathodic interface, the following electrochemical reaction

occurs:

$$2H^{+}+2e^{-}\rightarrow 2H_2$$

Prior to reaching the high-voltage threshold, a gradual increase in the applied voltage intensifies energy accumulation at the anode interface. This promotes bubble nucleation and growth, resulting in the formation of a continuous, stable gaseous insulating layer on the workpiece surface. This gas film effectively isolates the electrode from the polishing solution, thereby increasing the overall circuit resistance. As a result, the current initially rises to a peak and subsequently decays, marking the onset of the polishing transition stage.

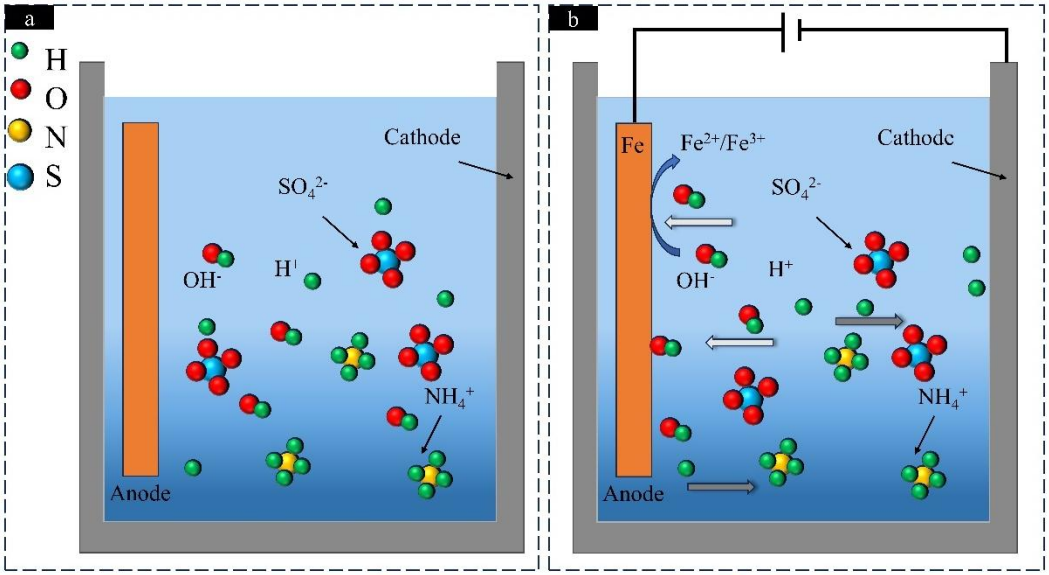


Fig. 2 Schematic illustration of bubble formation during electrochemical corrosion

(a) State of static equilibrium

(b) Ion migration upon application of an electric field

(2) Polishing transition phase — Bubble collapse and impact

In the polishing transition stage, significant heat accumulation occurs at the anode surface region owing to the Joule heating effect. This triggers localized boiling of the adjacent polishing solution, resulting in bubble generation and their subsequent coalescence into a vapor-gas layer. To elucidate the impact of bubble collapse on the workpiece surface, an analysis of the collapse mechanism of an individual bubble is presented. As bubbles nucleate in a high-temperature, high-energy environment, the

coalesced vapor-gas layer commonly comprises electrons, electrolyte ions, and metal ions derived from anodic dissolution. Driven by the elevated temperature, the internal pressure within the bubble increases swiftly, causing a transient volumetric expansion, as illustrated in Fig. 3-a. During the expansion phase, the internal bubble pressure gradually declines, leading to a deceleration of the expansion rate until a pressure equilibrium between the inside and outside of the bubble is established. The moment of rapid bubble expansion generates high-intensity shock waves in the surrounding liquid. A portion of this energy is dissipated within the polishing solution, while the remainder, upon reflection from interfaces, returns to compress the bubble, as illustrated in Fig. 3-b. This compression wave causes the internal bubble pressure to drop below the external hydrostatic pressure, inducing inward bubble collapse. This reduces the volume and subsequently increases the internal pressure. Once the internal pressure surpasses the external fluid pressure, further collapse is counteracted, ultimately resulting in bubble implosion, as depicted in Fig. 3-c. During bubble implosion, anions from the vapor-gas layer are transported to the anode surface, propelled by both the electric field and shock waves, where they interact with cations dissolved from the metal. Concurrently, the micro-jets and impact forces resulting from the bubble collapse impose a localized mechanical action on the metal surface, as illustrated in Fig. 3-d.

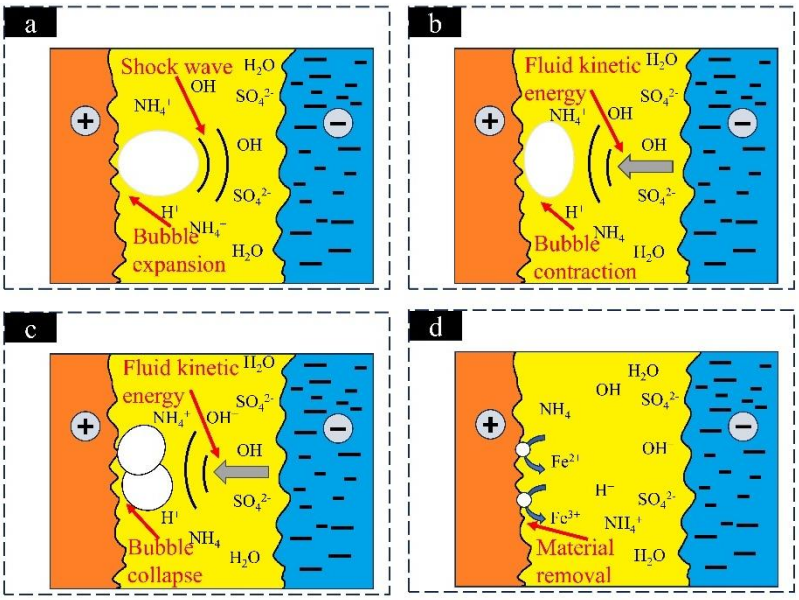


Fig. 3 Schematic illustration of the bubble implosion process

(a) Bubble expansion (b) Bubble contraction

(c) Bubble implosion (d) Material removal

(3) Formation of discharge channels — Gas layer ionization

With increasing voltage, the polishing process transitions into the gas layer ionization stage, as illustrated in Fig. 4. Breakdown of the gas layer occurs when its thickness results in a substantial voltage drop across it, leading to the generation of electrons and positive ions. Owing to their low mass, electrons are accelerated rapidly toward the anode (the workpiece surface) by the electric field. The heavier positive ions and neutral particles migrate more slowly, effectively forming a quasi-stationary space charge within the gas layer [25], as depicted in Fig. 4-a. The high-velocity electrons collide with neutral species in the gas layer, inducing ionization and photon emission. These photons, in turn, excite other neutrals to emit secondary electrons, resulting in an avalanche multiplication of electrons—a process termed an electron avalanche, as shown in Fig. 4-b. As the electric field produced by the accumulated space charge nears the intensity of the external field, field distortion occurs, leading to the formation of an initial discharge channel. Discharge channels preferentially initiate at surface asperities where the gas layer is thinner and the local electric field is enhanced, as illustrated in Fig. 4-c. The increase in charge carrier density within the channel intensifies particle collisions, raising its temperature and converting it into a plasma channel. High-energy electrons within the plasma continuously bombard the surface, inducing localized melting. Simultaneously, the self-induced magnetic field compresses the channel inward via the "pinch effect," further constricting and heating the plasma. The interplay between gas expansion and magnetic compression triggers localized micro-explosions. The resulting cavitation effect dislodges the molten surface material, as shown in Fig. 4-d. Throughout this process, the metal surface is continuously oxidized, and the oxides formed are concurrently removed. This creates a dynamic balance between oxidation and material removal, which effectively erases surface irregularities, blunts sharp edges, eliminates burrs, and results in global surface planarization.

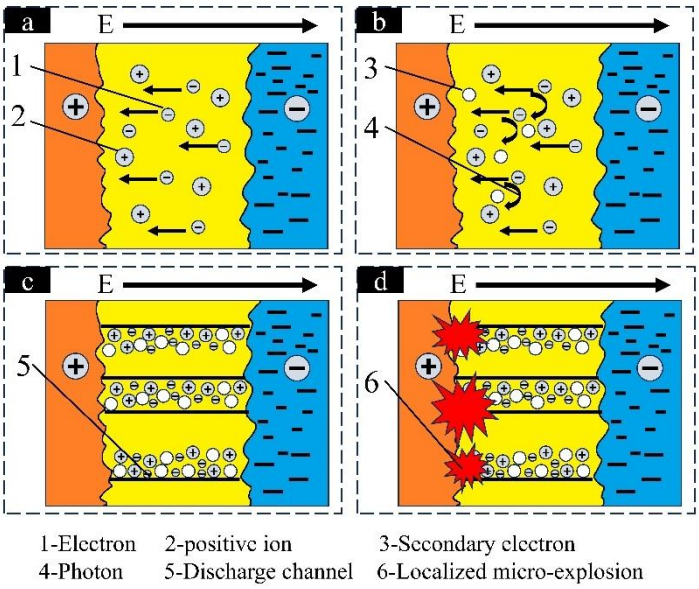


Fig. 4 Schematic illustration of the gas layer ionization process

3. Simulation and analysis of electrolyte plasma polishing

3.1 Electric and flow field simulation

3.1.1 Mathematical model

During electrolytic plasma polishing (EPP), the generated heat and gaseous products alter the electrical conductivity of the electrolyte and the local current density in the machining zone, which subsequently impacts the processing precision and stability. In practice, however, the electrolyte temperature is regulated by forced circulation, resulting in minimal temperature variation across the machining zone. Hence, the electrolyte temperature T is assumed to be spatially uniform [26]. This work assumes the electrolyte is maintained at a preset constant temperature T_0. Thus, the effect of electrolyte temperature fluctuation on the process is neglected, and the analysis focuses exclusively on the influence of the electric and flow fields.

(1) Electric field modeling

Electrolytic plasma polishing operates at voltages as high as approximately 380 V. Consequently, the electric field distribution within the polishing cell is highly dependent on the spatial configurations of both the gas layer and the electrolyte. Given that the electrolyte is a dilute salt solution, the effect of concentration polarization on the potential distribution is negligible [26]. Assuming the polishing solution is isotropic, and based on the law of charge conservation and Ohm's law, the electric field distribution satisfies the Laplace equation, i.e.:

$$\frac{\partial^2 \varphi}{\partial x^2} + \frac{\partial^2 \varphi}{\partial y^2} + \frac{\partial^2 \varphi}{\partial z^2} = 0 \tag{1}$$

The electric field strength at any spatial location is equal to the negative gradient of the electric potential at that point, i.e.:

$$E = -\nabla \varphi \tag{2}$$

Since both the anode and cathode in electrolytic plasma polishing are metallic, their potential distributions can be treated as equipotential surfaces. Thus, the boundary condition on the anode surface is defined as:

$$\varphi_a = U \tag{3}$$

And the boundary condition on the cathode surface is:

$$\varphi_c = 0 \tag{4}$$

The electric field mathematical model constructed for the polishing process is:

$$\begin{cases} \dfrac{\partial^2 \varphi}{\partial x^2} + \dfrac{\partial^2 \varphi}{\partial y^2} + \dfrac{\partial^2 \varphi}{\partial z^2} = 0 \\ E = -\nabla \varphi \end{cases} \tag{5}$$

(2) Flow field modeling

The development of the flow field mathematical model for the polishing process is based on the following premises: ① the polishing solution is modeled as an incompressible, steady-state fluid with constant viscosity; ② the flow field adheres to the momentum conservation law, and thermal effects are disregarded. Under these assumptions, the momentum-conserving Navier-Stokes equations for a viscous, incompressible fluid [27] are employed to describe the flow field characteristics of the polishing solution during processing.

$$\rho u \cdot \nabla u = \nabla[-PI + \eta(\nabla u + (\nabla u)^T)] + F \tag{6}$$

where: ρ denotes the electrolyte density; u represents the flow velocity; ∇ is the gradient operator; P indicates the fluid pressure; I is the identity tensor; η stands for the dynamic viscosity; F signifies the body force. The body force acting on the electrolyte is typically negligible in polishing operations.

The kinematic viscosity coefficient is defined as:

$$\eta = \frac{P_v}{v} \tag{7}$$

where v denotes the kinematic viscosity, a temperature-dependent parameter. The viscous friction pressure loss for the polishing solution is given by:

$$P_v = \lambda \frac{L}{D_h} \cdot \frac{\rho u_0^2}{2} \tag{8}$$

where L represents the flow length across the gap, D_h is the hydraulic diameter, and $\lambda = \frac{0.3164}{R_e^{0.25}}$. Since the electrolyte flow is turbulent during polishing, the Reynolds number Re is set to 2300 [28,29]. u_0 is the inlet flow velocity of the electrolyte.

Boundary conditions for the flow field: The inlet is specified with a total pressure P_0, where $P_0 = P_u + P_d + P_e$. The dynamic pressure is $P_d = \frac{\rho u_0^2}{2}$. The outlet is

prescribed with a back pressure P_e.

The constructed mathematical model for the polishing solution flow field is:

$$\begin{cases} \rho u \cdot \nabla u = \nabla[-PI + \eta(\nabla u + (\nabla u)^T)] + F \\ \eta = \dfrac{P_v}{v} \\ P_v = \lambda \dfrac{L}{D_h} \cdot \dfrac{\rho u_0^2}{2} \\ P_0 = P_u + P_d + P_e \\ P_d = \dfrac{\rho u_0^2}{2} \\ P = P_e \end{cases} \tag{9}$$

3.1.2 Simulation process

The finite element analysis method was adopted to simulate the electric field and flow field in the electrolytic plasma polishing process. To improve computational efficiency, the solution domain was restricted to a region 4-8 times larger than the specimen, given that the predominant voltage drop occurs across the gas layer and the flow field is confined by the apparatus and fixture configuration. Simplified models were constructed as illustrated in Fig. 5. For the electric field simulation (a), the model includes a workpiece and a rectangular parallelepiped electrolyte domain. The flow field model (b) contains a workpiece and a cylindrical electrolyte domain. The workpiece material was high-strength steel, the cathode was copper, and the electrolyte was an aqueous solution of ammonium sulfate with a concentration of 4 wt.%, held at a constant temperature of 85°C. Key parameters used in the simulations are summarized in Table 1.

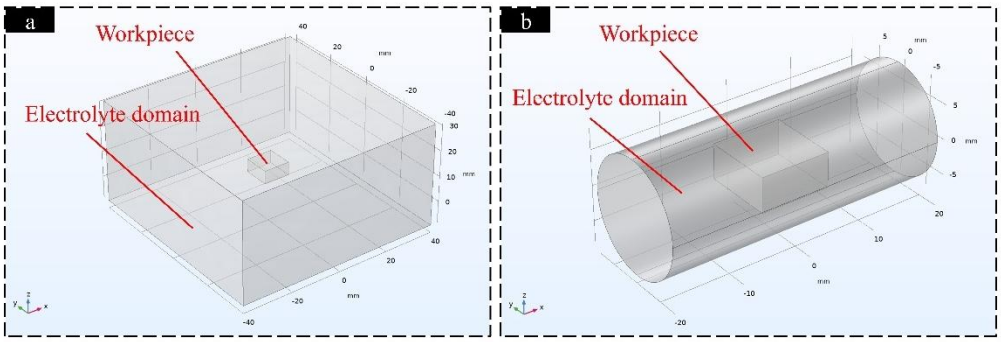


Fig. 5 Schematic diagram of the simplified model for electrolyte plasma

polishing

(a) Geometric model of the electric field

(b) Geometric model of the flow field

Table 1 Simulation parameters for the electric and flow field models

Parameters	Value
Anode voltage/V	300
Anode conductivity/(S • m^{-1})	1.38×10^6
Anode relative permittivity	1×10^6
Cathode voltage/V	0
Cathode conductivity/(S • m^{-1})	1.38×10^6
Cathode relative permittivity	1×10^6
Electrolyte conductivity /(S • m^{-1})	10
Electrolyte relative permittivity	55
Dynamic viscosity /(Pa • s)	1.03
Inlet pressure /MPa	0.2
Outlet pressure /MPa	0.01

An initial physics-controlled mesh was generated, and the element size was subsequently adjusted to improve solution accuracy. To ensure mesh independence, three distinct mesh densities were evaluated: a coarse mesh (I), a standard mesh (II), and a fine mesh (III). All three meshes shared identical settings for the maximum element growth rate, curvature factor, resolution of narrow regions, and initial conditions. For each mesh, the steady-state distribution of the electric field norm on the workpiece surface was simulated. The maximum and minimum values of the field norm on the side surface were then extracted and compared. The results, presented in Table 2, indicate a substantial difference between meshes I and II, with a 31.3% relative error in the maximum electric field norm, while the minimum values were nearly the same. The discrepancy between meshes II and III was smaller, showing an 11.7% error in the maximum norm, and the minimum values were in agreement. Moreover, the computational time for mesh II was reduced by about 50% compared to mesh III.

Considering its favorable trade-off between computational cost and accuracy, mesh II was adopted for all subsequent numerical simulations in this work.

Table 2 Mesh independence analysis

	Mesh I	Mesh II	Mesh III
Max element size/mm	1	0.7	0.6
Min element size /mm	0.7	0.6	0.5
Max element growth rate	1.1	1.1	1.1
Curvature factor	0.3	0.3	0.3
Resolution of narrow regions	1	1	1
Degrees of Freedom	5999501	17529479	27852747
Computation Time /S	43	127	214
Max electric field norm /(KV/m)	72.8	106	120
Min electric field norm /(KV/m)	19.1	19.2	19.2

3.1.3 Analysis of simulation results

(1) Electric field characteristics of the electrolytic plasma polishing process

Fig. 6 shows the distribution of electric potential and electric field within the electrolyte solution domain. As can be seen from Fig. 6-a, the potential drop in the external polishing solution region is primarily concentrated near the specimen and gradually attenuates with increasing distance from it. This distribution pattern aligns with the voltage distribution characteristics in actual polishing processes where the specimen acts as the anode and the electrolytic cell as the cathode. Fig. 6-b indicates that the electric field strength around the specimen is relatively uniformly distributed overall, with values stably ranging between 20 and 60 kV/m. This suggests a strong consistency in current density distribution in this region, which is conducive to achieving uniform surface polishing. However, a significant increase in electric field strength is observed at the edges and corners of the specimen, where local field strength exceeds 140 kV/m. This phenomenon can be attributed to the electric field concentration effect caused by abrupt changes in geometric curvature. It may lead to an increased material removal rate at these locations, thereby adversely affecting the shape

accuracy of the specimen.

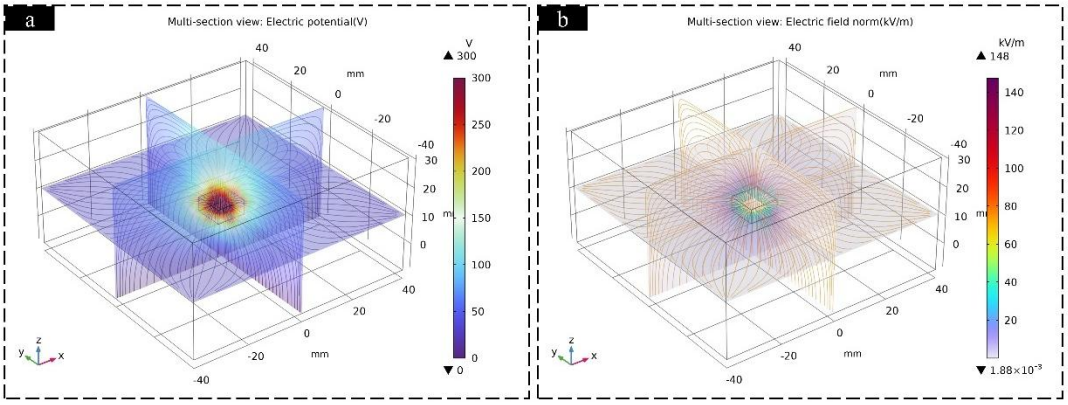


Fig. 6 Distribution of electric potential and electric field in the polishing solution domain

(a) Electric potential distribution

(b) Electric field distribution

(2) Flow field characteristics of the electrolytic plasma polishing process

A stable electrolyte flow is crucial for ensuring process stability during electrolytic plasma polishing. The flow field dictates the efficiency of by-product removal and the thermal distribution in the inter-electrode gap. To maintain process control, the electrolyte is often delivered at an elevated inlet pressure. The simulated flow field under steady-state conditions is presented in Fig. 7. As shown in Fig. 7-a, the electrolyte velocity field is largely uniform. A velocity decrease is mainly confined to the vicinity of the workpiece. Notably, localized vortices form in the wake of the workpiece, potentially degrading the polishing quality there. This flow pattern is consistent with the anticipated behavior for an anode (workpiece) and cathode (tank) configuration. Fig. 7-b further illustrates a gradual decline in flow velocity from the inlet to the outlet. High flow velocities promote efficient removal of reaction products and heat, contributing to process stability. However, flow obstruction in the workpiece wake reduces fluid motion, potentially impairing machining uniformity in that region.

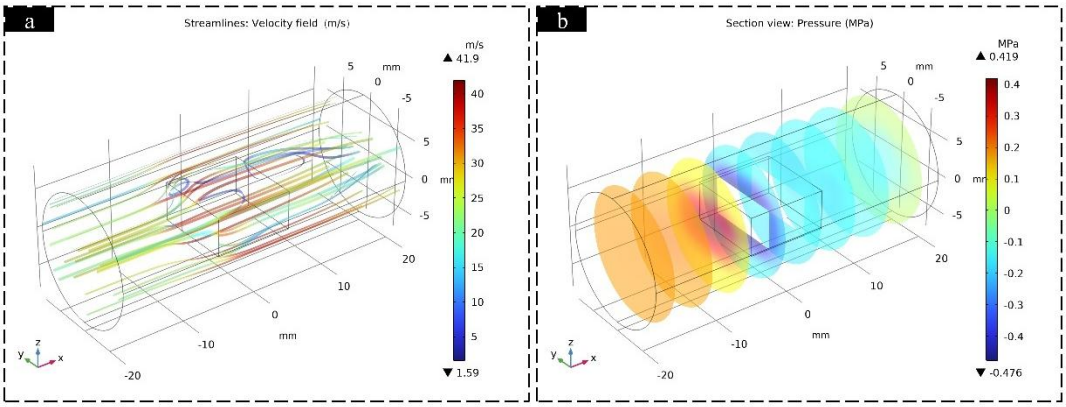


Fig. 7 Flow field distribution under steady-state polishing conditions

(a) Velocity field distribution

(b) Pressure cross-section distribution

3.2 Simulation of the gas layer formation process

3.2.1 Mathematical model

(1) Tertiary current distribution

The mathematical model for electrochemical transport is established on these premises: ① the electrolyte is a dilute solution where ion-ion interactions can be neglected; ② the system operates under isothermal, uniform-temperature conditions; ③ electroneutrality is rigorously maintained throughout the solution bulk. Under these assumptions, a set of governing equations is formulated to describe ion transport and charge conservation. This framework captures the coupled behavior of ionic concentration and electric field distributions in the electrochemical polishing process.

Mass conservation is governed by the Nernst-Planck equation:

$$\nabla \cdot \mathbf{j}_i + \mathbf{u} \cdot \nabla c_i = R_i \tag{10}$$

where $\mathbf{j}_i$ denotes the molar flux of ion i, c_i is its concentration, $\mathbf{u}$ represents the solution velocity, and R_i is the source/sink term due to homogeneous chemical reactions, accounting for the production or consumption rate of ion i.

Charge conservation is enforced in both the electrolyte and electrode phases as follows:

$$\nabla \cdot \mathbf{i}_l = F \sum_i z_i R_i + Q_l \tag{11}$$

$$\nabla \cdot \mathbf{i}_s = -F \sum_i z_i R_i + Q_s \tag{12}$$

where $\mathbf{i}_l$ denotes the current density in the electrolyte, $\mathbf{i}_s$ is the electrode current density, F is Faraday's constant, z_i is the charge number of ion i, and Q_l, Q_s are source terms for interfacial electrochemical reactions, accounting for the charge transfer rate across the electrode-electrolyte interface.

Electroneutrality ensures a balance of positive and negative charges in the bulk electrolyte:

$$\sum_i z_i c_i = 0 \tag{13}$$

This assumption obviates the need for solving the Poisson equation, thereby greatly reducing computational complexity.

The ionic flux is governed by a combination of diffusion and electromigration:

$$\mathbf{j}_i = -D_i \nabla c_i - z_i \mu_{m,i} F c_i \nabla \phi_l \tag{14}$$

where D_i denotes the diffusion coefficient of ion i, $\mu_{m,i}$ is its electrochemical mobility, and ϕ_l represents the electric potential in the electrolyte.

The current density is computed from the coupled contributions of the ionic fluxes:

$$\mathbf{i}_l = F \sum_i z_i \mathbf{j}_i \tag{15}$$

The electrode current obeys Ohm's law:

$$\mathbf{i}_s = -\sigma_s \nabla \phi_s \tag{16}$$

where σ_s denotes the electrode electrical conductivity, and ϕ_s is the electrode potential.

The boundary conditions are specified as: the electrode surface is governed by an electrochemical reaction kinetic boundary, commonly expressed using the Butler-Volmer equation; the electrolyte inlet has defined ion concentrations and flow velocity; an outflow condition is applied at the outlet; and insulating walls impose a zero normal flux condition.

The complete set of governing equations for the electrochemical transport model is thus established:

$$\begin{cases} \nabla \cdot \mathbf{j}_i + \mathbf{u} \cdot \nabla c_i = R_i \\ \nabla \cdot \mathbf{i}_l = F \sum_i z_i R_i + Q_l \\ \nabla \cdot \mathbf{i}_s = -F \sum_i z_i R_i + Q_s \\ \sum_i z_i c_i = 0 \\ \mathbf{j}_i = -D_i \nabla c_i - z_i \mu_{m,i} F c_i \nabla \phi_l \\ \mathbf{i}_l = F \sum_i z_i \mathbf{j}_i \\ \mathbf{i}_s = -\sigma_s \nabla \phi_s \end{cases} \tag{17}$$

(2) Bubbly flow

The mathematical model for gas-liquid two-phase turbulent flow is developed based on these premises: ① an Eulerian-Eulerian (two-fluid) framework is adopted; ② the liquid is treated as a continuous phase and the gas as a dispersed bubble phase; ③ the flow is fully turbulent, with liquid-phase turbulence described by the standard k-ε model; ④ bubble-turbulence interactions are accounted for. Guided by these assumptions, a set of governing equations is formulated to describe the two-phase turbulent flow, capturing the coupling between bubble transport and turbulent features in the plasma polishing process.

Conservation of momentum for the liquid phase is governed by the Reynolds-averaged Navier-Stokes (RANS) equations:

$$\phi_l \rho_l (\mathbf{u}_l \cdot \nabla) \mathbf{u}_l = \nabla \cdot [-p\mathbf{I} + \mathbf{K}] + \phi_l \rho_l \mathbf{g} + \mathbf{F} \tag{18}$$

where ϕ_l denotes the liquid volume fraction, ρ_l the liquid density, $\mathbf{u}_l$ the liquid velocity vector, p the pressure, $\mathbf{I}$ the identity tensor, $\mathbf{K}$ the Reynolds stress tensor, $\mathbf{g}$ the gravitational acceleration, and $\mathbf{F}$ the interphase momentum exchange term.

The overall mass balance is enforced by the mixture continuity equation:

$$\nabla \cdot \left(\phi_l \rho_l \mathbf{u}_l + \phi_g \rho_g \mathbf{u}_g \right) = 0 \tag{19}$$

where ϕ_g denotes the gas volume fraction (with $\phi_l + \phi_g = 1$), ρ_g is the gas

density, and $\mathbf{u}_g$ is the gas velocity vector.

The Reynolds stress tensor is closed via the Boussinesq hypothesis:

$$\mathbf{K} = \phi_l(\mu_l + \mu_T)\left(\nabla\mathbf{u}_l + (\nabla\mathbf{u}_l)^T - \frac{2}{3}(\nabla\cdot\mathbf{u}_l)\mathbf{I}\right) - \frac{2}{3}\phi_l\rho_l k\mathbf{I} \tag{20}$$

where μ_l denotes the molecular viscosity of the liquid, μ_T represents the turbulent (eddy) viscosity, and k is the turbulent kinetic energy.

The transport of bubbles is governed by the gas-phase continuity equation:

$$\nabla\cdot\left(\phi_g\rho_g\mathbf{u}_g\right) = -m_{gl} \tag{21}$$

where m_{gl} denotes the interphase mass transfer rate between the gas and liquid.

The gas velocity is obtained from a drift-flux model, which relates it to the mixture velocity:

$$\mathbf{u}_g = \mathbf{u}_l + \mathbf{u}_{slip} - \frac{D_{gc}}{\phi_g}\nabla\phi_g \tag{22}$$

$$D_{gc} = \frac{\mu_T}{\rho_l\sigma_T} \tag{23}$$

where $\mathbf{u}_{slip}$ denotes the bubble slip velocity, D_{gc} the bubble dispersion coefficient, and σ_T the turbulent Schmidt number.

The transport equation for turbulent kinetic energy includes a source term due to bubble-induced turbulence:

$$\rho_l(\mathbf{u}_l\cdot\nabla)k = \nabla\cdot\left[\left(\mu_l + \frac{\mu_T}{\sigma_k}\right)\nabla k\right] + P_k - \rho_l\epsilon + S_k \tag{24}$$

where σ_k is the turbulent Prandtl number for kinetic energy, P_k denotes the shear production of turbulence, ϵ is the turbulent dissipation rate, and S_k represents the source term due to bubble-induced turbulence.

The transport equation for the turbulent dissipation rate incorporates a term to account for bubble modulation:

$$\rho_l(\mathbf{u}_l\cdot\nabla)\epsilon = \nabla\cdot\left[\left(\mu_l + \frac{\mu_T}{\sigma_\epsilon}\right)\nabla\epsilon\right] + C_{\epsilon1}\frac{\epsilon}{k}P_k - C_{\epsilon2}\rho_l\frac{\epsilon^2}{k} + C_\epsilon S_k\frac{\epsilon}{k} \tag{25}$$

where σ_ϵ is the turbulent Prandtl number for the dissipation rate, and $C_{\epsilon1}, C_{\epsilon2}, C_\epsilon$ are empirical model constants.

The models for turbulent viscosity and the source terms are closed as follows:

$$\mu_T = \rho_l C_\mu \frac{k^2}{\epsilon} \tag{26}$$

$$S_k = -C_k \phi_g \nabla p \cdot \mathbf{u}_{slip} \tag{27}$$

where C_μ and C_k denote empirical model constants.

The exact expression for the shear production of turbulent kinetic energy is given by:

$$P_k = \mu_T \left[\nabla \mathbf{u}_l : (\nabla \mathbf{u}_l + (\nabla \mathbf{u}_l)^T) - \frac{2}{3}(\nabla \cdot \mathbf{u}_l)^2\right] - \frac{2}{3}\rho_l k \nabla \cdot \mathbf{u}_l \tag{28}$$

The following boundary conditions are applied: the inlet is prescribed with liquid velocity, gas volume fraction, and turbulence parameters; a fully developed flow condition is set at the outlet; no-slip conditions are imposed on walls, with near-wall flow resolved using standard wall functions.

The complete set of governing equations constituting the gas-liquid two-phase turbulent flow model is thus established:

$$\begin{cases} \phi_l \rho_l (\mathbf{u}_l \cdot \nabla)\mathbf{u}_l = \nabla \cdot [-p\mathbf{I} + \mathbf{K}] + \phi_l \rho_l \mathbf{g} + \mathbf{F} \\ \nabla \cdot \left(\phi_l \rho_l \mathbf{u}_l + \phi_g \rho_g \mathbf{u}_g\right) = 0 \\ \mathbf{K} = \phi_l(\mu_l + \mu_T)\left(\nabla \mathbf{u}_l + (\nabla \mathbf{u}_l)^T = \frac{2}{3}(\nabla \cdot \mathbf{u}_l)\mathbf{I}\right) - \frac{2}{3}\phi_l \rho_l k \mathbf{I} \\ \nabla \cdot \left(\phi_g \rho_g \mathbf{u}_g\right) = -m_{gl} \\ \mathbf{u}_g = \mathbf{u}_l + \mathbf{u}_{slip} - \frac{D_{gc}}{\phi_g}\nabla \phi_g \\ D_{gc} = \frac{\mu_T}{\rho_l \sigma_T} \\ \rho_l (\mathbf{u}_l \cdot \nabla)k = \nabla \cdot \left[\left(\mu_l + \frac{\mu_T}{\sigma_k}\right)\nabla k\right] + P_k - \rho_l \epsilon + S_k \\ \rho_l (\mathbf{u}_l \cdot \nabla)\epsilon = \nabla \cdot \left[\left(\mu_l + \frac{\mu_T}{\sigma_\epsilon}\right)\nabla \epsilon\right] + C_{\epsilon 1}\frac{\epsilon}{k}P_k - C_{\epsilon 2}\rho_l \frac{\epsilon^2}{k} + C_\epsilon S_k \frac{\epsilon}{k} \\ \mu_T = \rho_l C_\mu \frac{k^2}{\epsilon} \\ S_k = -C_k \phi_g \nabla p \cdot \mathbf{u}_{slip} \\ P_k = \mu_T \left[\nabla \mathbf{u}_l : (\nabla \mathbf{u}_l + (\nabla \mathbf{u}_l)^T) - \frac{2}{3}(\nabla \cdot \mathbf{u}_l)^2\right] - \frac{2}{3}\rho_l k \nabla \cdot \mathbf{u}_l \end{cases} \tag{29}$$

3.2.2 Simulation process

To better simulate the gas layer formation process, a computational domain as shown in Fig. 8 was established based on the electric and flow field simulation models, where Fig. 8-a depicts the geometric model and Fig. 8-b shows the meshing results.

The left and right boundaries, which are parallel, represent the cathode and anode surfaces. As the anode surface continually produces bubbles during polishing, the right boundary functions concurrently as a gas-phase inlet. The top boundary is defined as the liquid-phase inlet and gas-phase outlet, and the bottom boundary is assigned as the liquid-phase outlet. Key simulation parameters are summarized in Table 3.

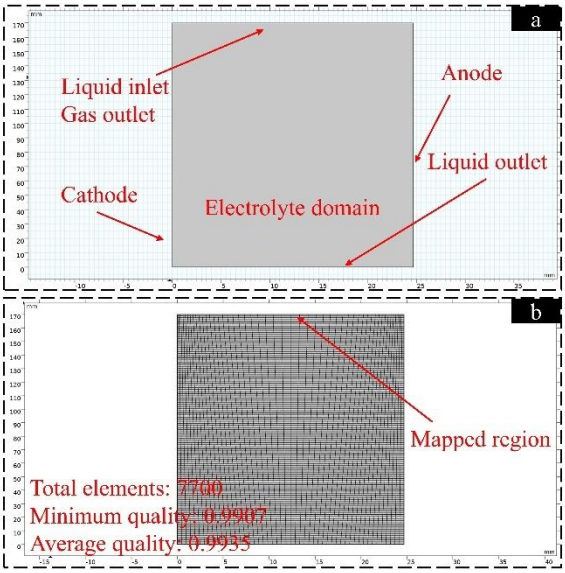


Fig. 8 Simulation model for the gas layer formation process

(a) Geometric model

(b) Mesh generation result

Table 3 Simulation parameter table for the gas layer formation process

Parameters	Value
Conductivity of $(NH_4)_2SO_4$ solution/(S/m)	10
Initial concentration of H^+/(mol/m^3)	1837
Initial concentration of OH^-/(mol/m^3)	1837
Diffusion coefficient of Fe/(m^2/s)	7.2E-10
Diffusion coefficient of H^+/(m^2/s)	9.31E-9
Diffusion coefficient of OH^-/(m^2/s)	5.31E-9
Standard equilibrium potential of Fe/V	-0.44
Exchange current density for Fe/(A/m^2)	10
Standard equilibrium potential of O_2/V	1.23

Exchange current density for O_2/(A/m²)	3E-7
Standard equilibrium potential of H_2/V	0
Exchange current density for H_2/(A/m²)	1E-4
Density of the electrolyte/(kg/m³)	1200
Viscosity of the electrolyte/(kg/(m • s))	8.35E-4
Molar mass of O_2/(kg/mol)	0.032
Bubble diameter/m	1E-5
Inlet velocity/(m/s)	0.01
Anode voltage/V	380

3.2.3 Analysis of simulation results

Fig. 9 presents the evolution of gas generation at the anode surface over time. Individual panels show the gas volume fraction and its spatial distribution at different observation instants. During the initial phase (0.5 s), gas nucleation and accumulation commence at the anode surface. The maximum and minimum volume fractions are 0.0695% and nearly negligible, respectively, reflecting a low concentration without notable spatial clustering. Over time, the gas volume fraction rises progressively, showing a distribution pattern that extends outward from the anode surface. At 20 s, the maximum volume fraction reaches 0.439%, demonstrating the ongoing accumulation of gas and the progressive establishment of a stabilized gas layer on the anode.

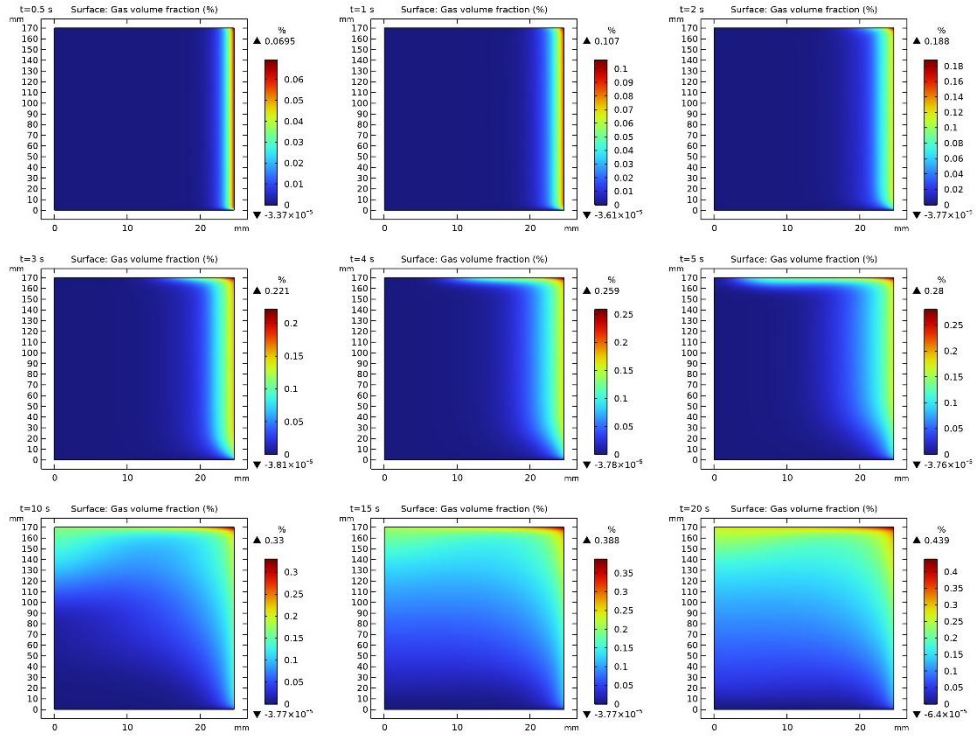


Fig. 9 Time-dependent evolution of gas generation at the anode surface

3.3 Simulation of the "peak removal" process

3.3.1 Mathematical model

The electromagnetic field model for the "peak removal" process is established based on these premises: ① the medium is linear and isotropic with time-invariant electromagnetic properties; ② the electromagnetic field obeys charge conservation and is governed by the quasistatic approximation. Under these assumptions, the electromagnetic field governing equations, which describe the current density distribution, are formulated. These equations capture the inherent coupling between electrode surface evolution and charge transport in the electrochemical system.

The generalized current continuity equation is given by:

$$\nabla \cdot \mathbf{J} = Q_{j,v} \tag{30}$$

where $\mathbf{J}$ denotes the total current density, and $Q_{j,v}$ is the volumetric current source term, characterizing the rate of charge generation or consumption per unit volume.

The constitutive relation between current density and electric field is given by the

generalized Ohm's law:

$$\mathbf{J} = \sigma\mathbf{E} + \frac{\partial \mathbf{D}}{\partial t} + \mathbf{J}_e \tag{31}$$

where σ denotes the electrical conductivity of the medium, $\mathbf{E}$ is the electric field strength, $\mathbf{D}$ is the electric displacement field, and $\mathbf{J}_e$ signifies the external (impressed) current density, which accounts for charge transport driven by non-electromagnetic mechanisms.

The electric field is related to the electric potential gradient by:

$$\mathbf{E} = -\nabla V \tag{32}$$

where V denotes the scalar electric potential, which describes the potential energy landscape of the field. Employing the quasistatic approximation allows neglect of the displacement current, and the constitutive relation for the electric displacement is $\mathbf{D} = \varepsilon\mathbf{E}$, with ε being the permittivity of the medium.

Modeling the consumption of the anode material necessitates a moving boundary approach, as the geometry and consequently the current density distribution evolve over time. A simplified model for material removal is adopted, positing that the removal rate is proportional to the normal component of the current density at the electrode surface. The velocity U normal to the electrode surface is then expressed as:

$$U = -KJ_n \tag{33}$$

Here, K is the proportionality constant, and J_n represents the normal component of the current density.

Consequently, the total anode material removal $d(\Delta t)$ evolves with time according to:

$$d(\Delta t) = |U|\Delta \mathrm{t} = K|J_n|\Delta t \tag{34}$$

The boundary conditions for the electromagnetic field are defined as follows: a fixed potential V_0 (Dirichlet condition) is applied on the electrode surface; insulating walls impose a zero normal current density ($\mathbf{J} \cdot \mathbf{n} = 0$, Neumann condition); and both potential continuity and current continuity are enforced at interfaces between different media.

The complete set of equations constituting the electromagnetic field model for the

"peak removal" process is thus established as follows:

$$\begin{cases} \nabla \cdot \mathbf{J} = Q_{j,v} \\ \mathbf{J} = \sigma \mathbf{E} + \dfrac{\partial \mathbf{D}}{\partial t} + \mathbf{J}_e \\ \mathbf{E} = -\nabla V \\ \mathbf{D} = \varepsilon \mathbf{E} \\ U = -K J_n \\ d(\Delta t) = |U|\Delta \mathrm{t} = K|J_n|\Delta t \end{cases} \tag{35}$$

3.3.2 Simulation process

To simulate the "peak removal" process, a computational domain as shown in Fig. 10 was established based on the previous work, where Fig. 10-a depicts the geometric model and Fig. 10-b shows the meshing results. The left and right boundaries represent the cathode and anode surfaces, respectively. The anode surface incorporates several protrusions to simulate surface defects. The top and bottom boundaries are defined as electrically insulating. Key simulation parameters are listed in Table 4.

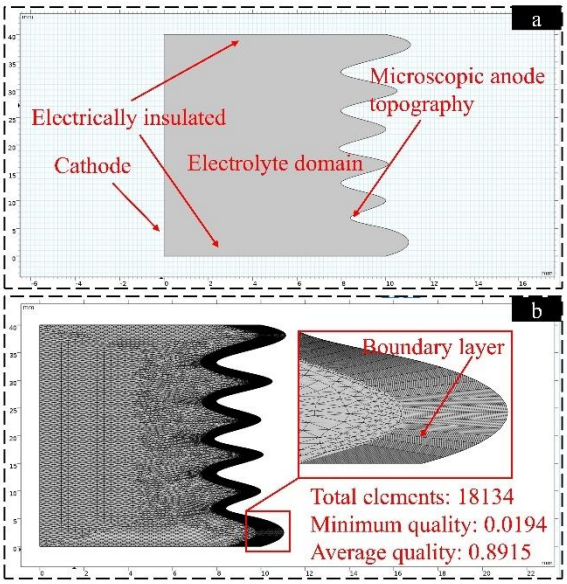


Fig. 10 Simulation model for the "peak removal" process

(a) Geometric model

(b) Mesh generation result

Table 4 Simulation parameter table for the "peak removal" process

Parameters	Value
Proportionality coefficient/(m³/(As))	1E-11

Conductivity of $(NH_4)_2SO_4$ solution/(S/m)	10
Dielectric constant of $(NH_4)_2SO_4$ solution	55
Anode voltage/V	380

3.3.3 Analysis of simulation results

Fig. 11 illustrates the time-dependent evolution of the anode surface microstructure. Each panel depicts the surface displacement distribution at a specific observation time. During the initial phase (0.1 min), the anode surface exhibits minimal change. With a maximum displacement of 0.103 mm and a minimum near zero, the deformation is limited, yet the peak-leveling mechanism has commenced. With continued polishing, the surface morphology is substantially reconfigured. After 15 min, the maximum displacement reaches 4.49 mm, indicating a pronounced enhancement of the peak-leveling effect. The original microscopic asperities on the anode are largely eradicated, and the overall profile is leveled.

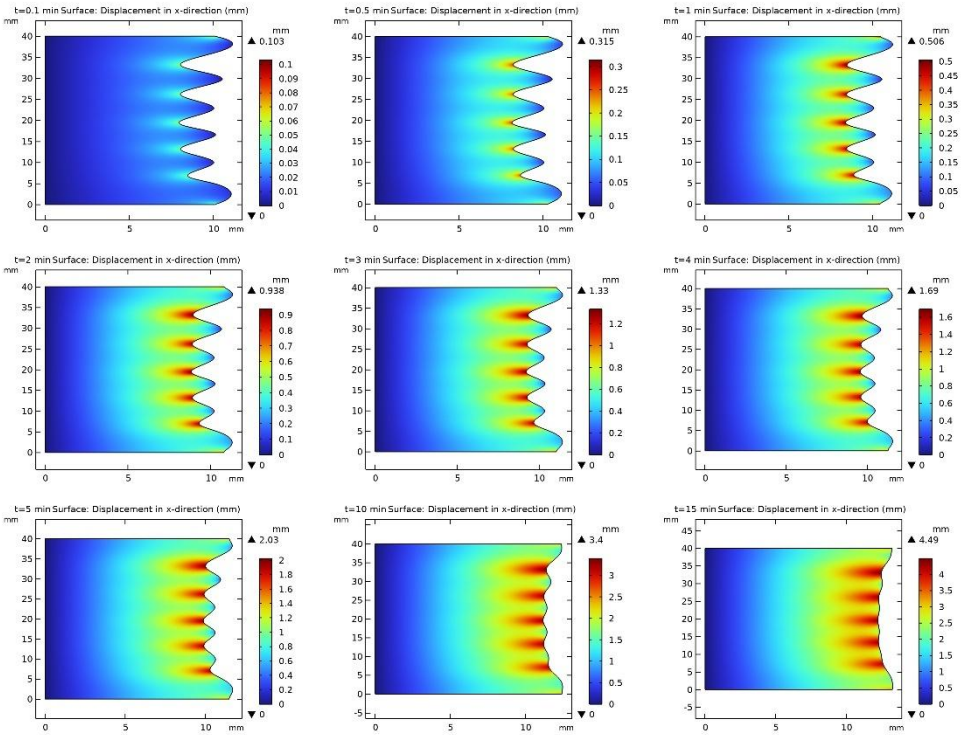


Fig. 11 Time-dependent evolution of the anode surface microstructure

4. Experimental validation and results analysis

4.1 Experimental validation

(1) Sample preparation

This study selected high-strength steel from the same batch of artillery barrel material for polishing experiments. Specimens, as shown in Fig. 12, were prepared via wire cutting with dimensions of 15mm × 15mm × 5mm. Their primary chemical composition is presented in Table 5 [5]. Considering that the specimen surface might be covered with an oxide layer and other impurities that could affect polishing results, and to ensure all specimens had the same surface roughness before polishing, the specimen surfaces were sequentially ground using 200#, 400#, and 800# grit sandpaper prior to the experiment. This process exposed the metallic luster and achieved a surface roughness of approximately 2.3 μm. Subsequently, ultrasonic cleaning and drying were performed.

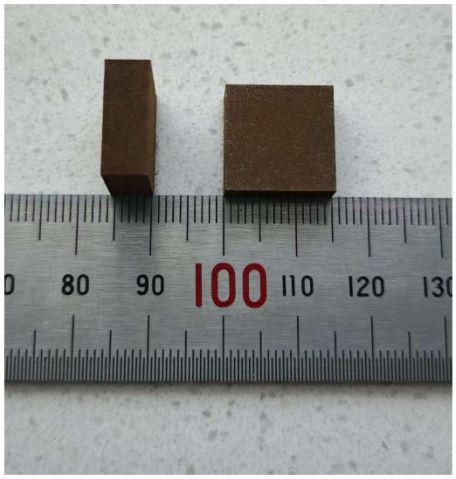


Fig. 12 Diagram of specimen sample prepared by wire cutting

Table 5 Chemical composition of the high-strength steel (wt%)

C	Mn	Si	Cr	Ni	Mo	V	S	P
0.40	0.41	0.25	1.28	3.14	0.37	0.20	0.001	0.012

(2) Construction of the test platform

The polishing test platform employed in this study was custom-designed and fabricated, as illustrated in Fig. 13-a. The platform is comprised of a DC power supply

system, a polishing electrolyte circulation system, a polishing electrolyte temperature control system, a polishing cell, and a sample holder. The DC power supply, rated at 20 kW, allows for the adjustment of key process parameters including the plasma polishing voltage and current. The polishing electrolyte circulation system, consisting of a 220V small pump and PVC tubing, facilitates rapid electrolyte flow. An intelligent temperature-controlled electric heater is employed in the temperature control system, providing real-time display and regulation of the electrolyte temperature. The polishing cell has a capacity of 10 liters. As shown in Fig. 13-b, the sample holder was monolithically printed using Bambu Lab PAHT-CF high-temperature resistant material to fulfill the multifunctional requirements of sample clamping, electrolyte sealing, electrical conductivity, and thermal resistance.

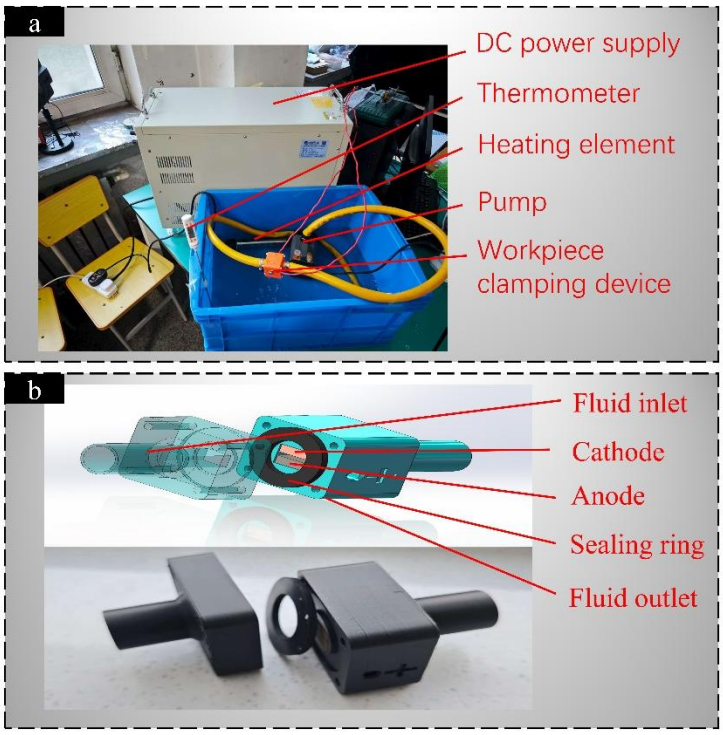


Fig. 13 Schematic of the polishing test platform design

The experimental procedure was conducted as follows: The sample to be polished was connected to the anode (positive terminal), and the polishing cell was connected to the cathode (negative terminal). The polishing electrolyte, prepared using deionized water as the solvent and pre-selected salts as solutes, was heated to a predetermined temperature within the polishing cell. The electrolyte circulation system was connected.

Upon reaching the target temperature, the circulation system was activated and the voltage was applied and adjusted. Following the polishing process, the sample surface was rinsed with deionized water, dried, and stored for subsequent use.

4.2 Analysis of experimental results

4.2.1 Surface morphology changes

(1) Macroscopic surface morphology

The macroscopic surface morphology of the high-strength steel specimen before and after the polishing process is compared in Fig. 14. The results reveal that the unpolished specimen surface contained significant defects including corrosion, pits, and machining traces, which compromised its surface integrity. Following polishing, the specimen surface displayed a uniform metallic sheen, a substantial reduction in macroscopic undulations, and an overall smoother topography, indicating a notable enhancement in surface finish and overall quality.

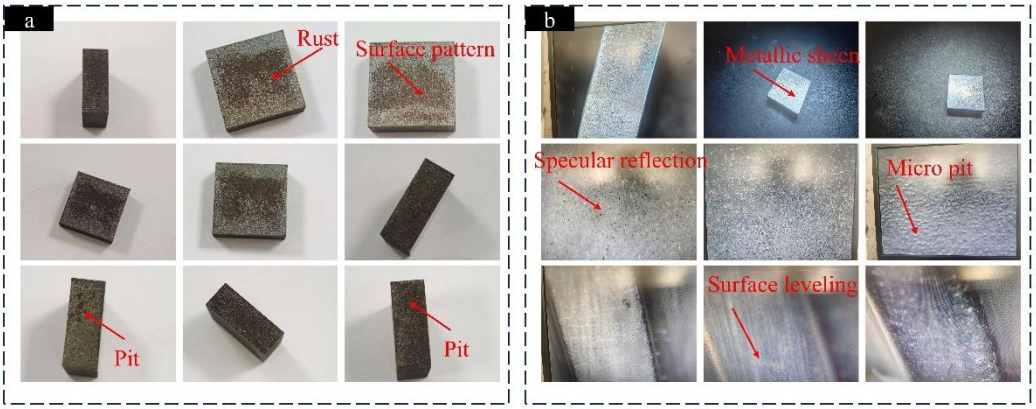


Fig. 14 Macroscopic morphology comparison of the high-strength steel surface before and after polishing

(a) Surface macroscopic morphology before polishing

(b) Surface macroscopic morphology after polishing

(2) Surface roughness

As shown in Fig. 15, the electrolytic plasma polishing process substantially improved the surface quality of the workpiece. The process markedly reduced the surface roughness (Ra) from an initial value of 2.370 μm to 0.879 μm, corresponding

to a decrease of 62.9%. This outcome confirms that the process effectively removes surface asperities and defects, thus resulting in a smoother surface topography.

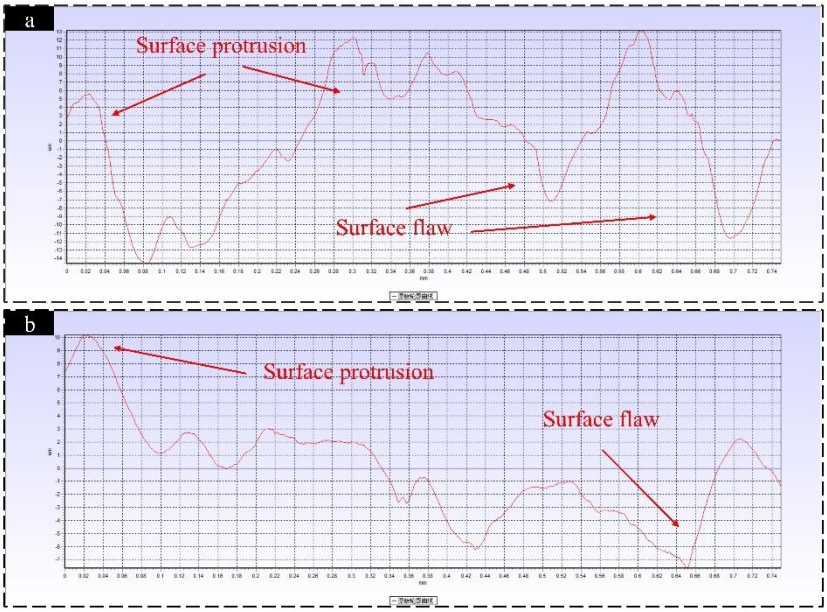


Fig. 15 Surface roughness measurement results for the high-strength steel before and after polishing

(a) Surface roughness curve before polishing

(b) Surface roughness curve after polishing

(3) Surface microstructure and morphology

Scanning electron microscopy (SEM) observations in Fig. 16 reveal that the original surface microstructure of the high-strength steel was markedly altered after the plasma polishing process. The initially dense network of micron-scale grooves was effectively leveled by the plasma interaction, with surface scratches being largely removed, leading to a notable improvement in overall surface smoothness.

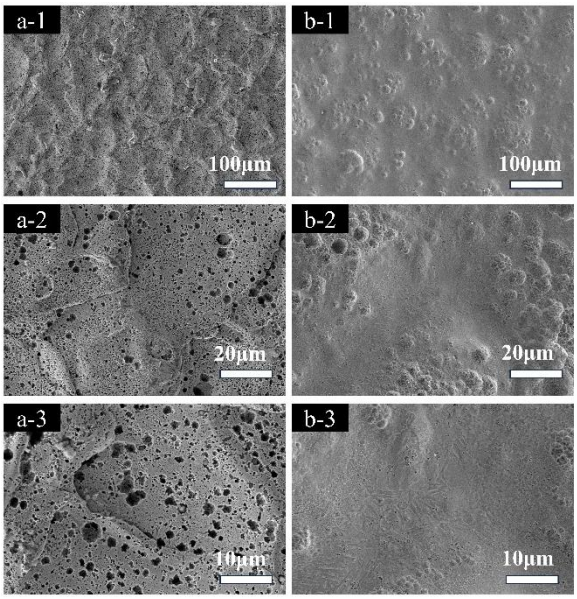


Fig. 16 Surface microstructure and morphology of the high-strength steel before and after polishing

(a) Microstructure and morphology of the unpolished surface

(b) Microstructure and morphology of the polished surface

(4) Surface 3D topography

The 3D surface topography of a 2.4 mm × 2.4 mm area on the specimen was characterized using laser scanning confocal microscopy before and after polishing, as presented in Fig. 17. The results indicate that the maximum peak-to-valley height (S z) was reduced from 57.8 μm to 47.2 μm, signifying a transition from pronounced macroscopic undulations to a notably smoother surface. The post-polishing microstructure exhibited fine-scale "asperities" or "protrusions" attributed to plasma bombardment and gas blasting effects. This resulted in a dual enhancement of surface quality, concurrently improving overall flatness and modifying the micro-scale surface architecture.

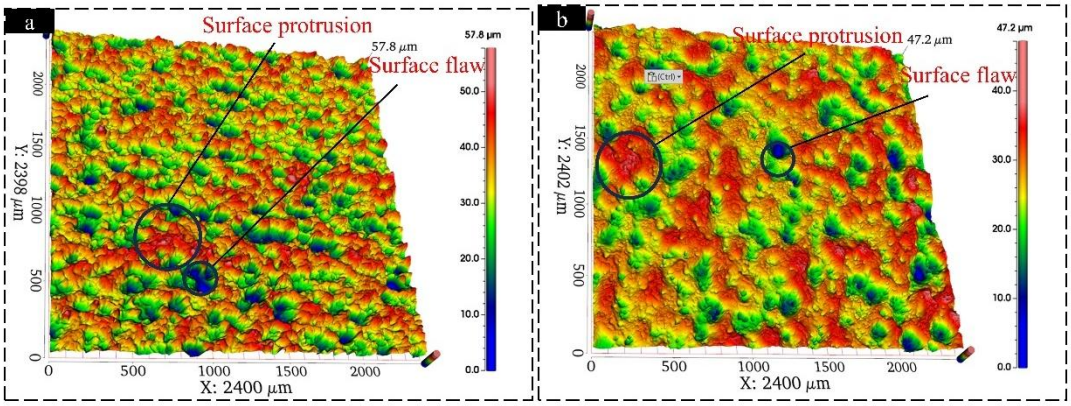


Fig. 17 3D surface topography of the high-strength steel before and after polishing

(a) 3D surface topography before polishing

(b) 3D surface topography after polishing

4.2.2 Surface elemental composition and hardness variations

(1) Surface elemental composition

Fig. 18 presents the EDS (Energy Dispersive X-ray Spectroscopy) spectra obtained from the high-strength steel surface prior to and following the electrolytic plasma polishing process. Variations in the surface elemental composition of the sample before and after polishing are illustrated in Fig. 19. Following the polishing treatment, the oxygen content on the specimen surface was markedly reduced, whereas the chromium (Cr) content exhibited a slight increase. This phenomenon can be attributed to the removal of surface oxides via plasma interaction during polishing. Concurrently, the chromium-depleted layer near the surface, characterized by its lower Cr content, is preferentially etched away. This results in the relative enrichment of the underlying chromium-rich layer at the surface, thereby increasing the measured Cr content.

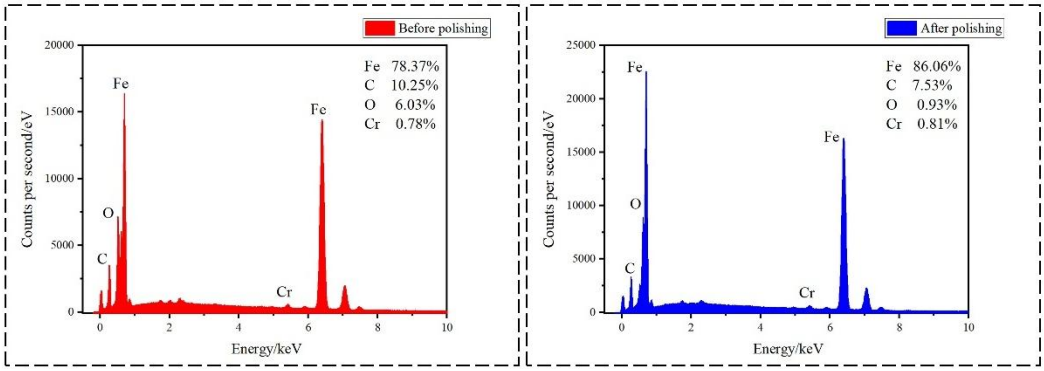


Fig. 18 EDS spectra of the high-strength steel surface before and after polishing

(a) EDS spectrum before polishing

(b) EDS spectrum after polishing

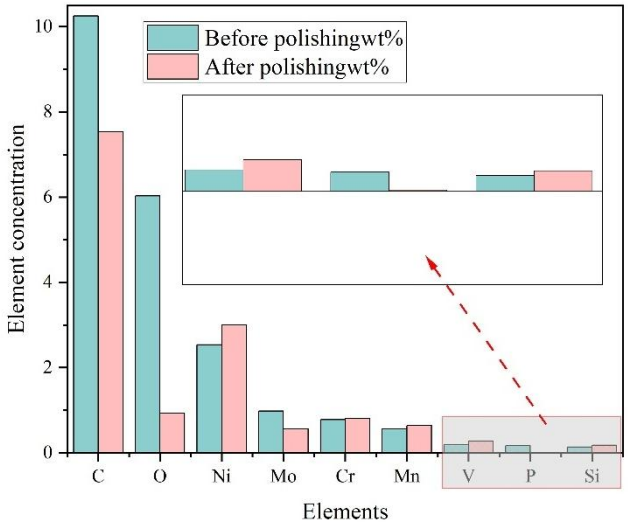


Fig. 19 Variation in surface elemental composition of the high-strength steel before and after plasma electrolytic polishing

(2) Surface hardness

Vickers hardness measurements were performed on the samples both before and after polishing. For statistical reliability, 15 indentation points were tested on each sample, and the results are presented in Fig. 20. The results indicate a modest decrease in the hardness of the high-strength steel following the polishing process. This reduction in hardness is attributed to the removal of the original surface layers possessing relatively higher hardness, including oxides, surface defects, and carbon-enriched layers, which were eroded by the plasma bombardment during processing.

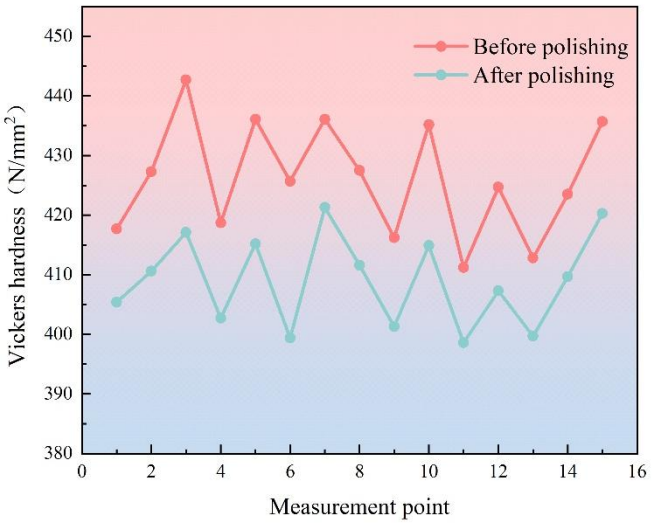


Fig. 20 Variation in surface Vickers hardness of the high-strength steel before and after polishing

5. Conclusions

(1) A multi-physics coupled simulation model incorporating the electric field, flow field, gas-liquid two-phase flow, and the peak removal process was developed to dynamically simulate the peak removal process initiated by electrochemical dissolution, bubble evolution, and collapse at the workpiece surface. The results indicate that the peak removal process is initiated by electrochemical dissolution along with concurrent bubble evolution and collapse at the surface. The mechanism responsible for material removal is attributed to the synergistic effects of fluid erosion, the formation of localized discharge channels, and discharge from the peaks of surface asperities.

(2) Analysis of the surface microstructure of the polished high-strength steel reveals a markedly enhanced surface finish, characterized by a distinct metallic luster and a substantial reduction in surface roughness. A decrease in the density of micro-scale surface undulations and a reduction in scratch count contribute to effective surface leveling, leading to a significantly improved microscopic topography.

(3) Following polishing, the surface oxygen content of the specimen decreased significantly, while the chromium content exhibited a marginal increase, accompanied by a slight reduction in microhardness. These results demonstrate that the polishing process leads to a significant enhancement in the surface characteristics of the high-strength steel.

Author contribution

Pengfei Li: Writing-original draft, Visualization, Formal analysis, Data curation. Feng Yang: Writing–review editing, Methodology, Supervision, Project administration, Funding acquisition, Conceptualization. Bingxin Liu: Resources. Xiankun Cheng: Validation and Investigation.

Funding

This study has been supported by the National Major Special Project Topics (HP20250105-03) and the Shenyang Natural Science Foundation of Liaoning Province of China (No. 23503604).

Data availability

The data used to support the findings of this study are available from the corresponding author upon request.

Declarations

Ethics approval Because the research of this paper belongs to the field of electrolyte plasma polishing technology, the research content of this paper does not involve ethical issues.

Consent to participate

All authors agree to participate in this manuscript.

Consent for publication

All authors agree to submit and publish this manuscript in *The International Journal of Advanced Manufacturing Technology* as a full-length article.

Conflict of interest

The authors declare no competing interests.

References

[1] Y.Q. Ma, X.Y. Su, H.Y. Wang, P.J. Zhang, J.D. Zhu. (2020). Study on Efficiency of Detection Device for Gun Barrel Bore. *Automation & Instrumentation*, DOI: 10.19557/j.cnki.1001-9944.2020.11.013.

[2] B.Q. Mao, Q.J. Zhao, X.H. Bai, Z.Q. Wang, R. Zhu, C.L. Chen. (2023). Review and Prospect of Life Extension Technology for Gun Barrels. *Acta Armamentarii*, DOI: 10.12382/bgxb.2021.0787.

[3] D.D. Li. (2024). Preparation and performance study of a novel coating for extending the life of gun barrel. *Master's Thesis, Shenyang Ligong University*, DOI: 10.27323/d.cnki.gsgyc.2024.000592.

[4] X.H. Geng, H.Y. Li, F.F. Liu, G. Tan, R.Q. Yang, Z.Y. Zhao, Y. Bing. (2024) Life test and inner bore damage analysis of high chamber pressure gun barrel. *Journal of Physics: Conference Series*, DOI: 10.1088/1742-6596/2891/14/142001.

[5] C.A. Guo, X. Jiang, X.L. Feng, Y.B. Ding. (2023). Influence of Temperature on Friction and Wear Performance of Chromium-plated Coating on Gun Steel. *Hot Working Technology*, DOI: 10.14158/j.cnki.1001-3814.20213093.

[6] X.D. Yuan, L.Q. Gao, H.F. Zhang. (2017). Development and Prospect of Gun Barrel Materials. *Development and Application of Materials*, DOI: 10.19515/j.cnki.1003-1545.2017.05.019.

[7] F.S. Yuan, C.Z. Liu, H.F. Gu, F.Z. Han, Y.D. Zhang, M. Ali, G.P. Li. (2019). Effects of mechanical polishing treatments on high cycle fatigue behavior of Ti-6Al-2Sn-4Zr-2Mo alloy. *International Journal of Fatigue*, DOI: https://doi.org/10.1016/j.ijfatigue.2018.12.003.

[8] J. Wang. (2013). Research on metal surface electrolysis and plasma polishing and process. *Doctoral Dissertation, Harbin Institute of Technology.*

[9] H.D. Duan, H.W. Sun, G.Q. Ji, D.L. Yang, S.X. Li, J. Wang, Y.X. Xiang. (2022). Biological corrosion resistance and osteoblast response of 316LVM polished using electrolytic plasma. *Coatings*, DOI: https://doi.org/10.3390/coatings12111672.

[10] T.T. Yan, S.Q. Wang, W.D. He, R. Jin, J.J. Zhao, Y.C. Zou, J.H. O.Y, Y.M.

Wang, Y. Zhou. (2025). Precision Machining of Different Metals by Plasma Electrolytic Polishing: A Review for Improving Surface Smoothness and Properties. *Lubricants*, DOI: https://doi.org/10.3390/lubricants13090412.

[11] H.D. Duan, H.W. Sun, G.Q. Ji, D.L. Yang, S.X. Li. (2022). Evolution of Chemical Speciation and Interfacial Reaction of Elements on the Surface of Stainless Steel during Electrolytic Plasma Polishing. *Surface Technology*, DOI: 10.16490/j.cnki.issn.1001-3660.2022.06.033.

[12] S.Y. Zhang. (2020). Key technique of inductively coupled plasma in polishing *Doctoral Dissertation, University of Chinese Academy of Sciences (Institute of Optics and Electronics, Chinese Academy of Sciences),* DOI: 10.27543/d.cnki.gkgdk.2020.000086.

[13] L.M. Wang. (2023). Application of electrolyte plasma in runner polishing and cross-hole deburring. *Master's Thesis, Harbin Institute of Technology,* DOI: 10.27061/d.cnki.ghgdu.2023.006731.

[14] Y.M. Liu. (2023). Research on mechanical grinding and electrolytic polishing composite processing technology of small diameter seamless pipe. *Master's Thesis, Taiyuan University of Science and Technology,* DOI: 10.27721/d.cnki.gyzjc.2023.000414.

[15] G.Q. Ji. (2023). Study on interface reaction mechanism of electrolytic plasma polishing for stainless steel. *Doctoral Dissertation, Taiyuan University of Technology,* DOI: 10.27352/d.cnki.gylgu.2023.000541.

[16] X.T. Yan, B.R. Wang, L. Wang, H. Y, C.X. Han. (2025). Jet electrolytic plasma polishing process for high temperature alloy additive manufacturing of large size surfaces. *AIP Advances,* DOI: https://doi.org/10.1063/5.0250696.

[17] J. Wang, L.C. Suo, L.L. Guan, Y.L. Fu. (2013). Regularity of surface roughness with polishing time in electrolysis and plasma polishing. *Journal of Harbin Engineering University,* DOI: 10.3969/j.issn.1006-7043.201203060.

[18] J. Wang, L.C. Suo, Y.L. Fu. (2014). Detecting the mass fraction of ammonium sulfate in polishing solution in electrolysis and plasma polishing. *Materials Science and Technology,* DOI: 10.11951/j.issn.1005-0299.20140206.

[19] Y.M. Yuan, H. Li, P.Y. Xie, H.Q. Wang, L. Hu, X.H. Ge. (2024). Effects of process parameters on electrolysis and plasma polishing of selective laser melted 316L stainless steel. *Electroplating & Finishing,* DOI: 10.19289/j.1004-227x.2024.03.009.

[20] J.X. Zai, H. Li, Y.M. Yuan, X.H. Ge. (2023). Study on electrolyte plasma polishing process of TC4 titanium alloy. *Electroplating & Finishing,* DOI: 10.19289/j.1004-227x.2023.10.006.

[21] S.H. Dai, J.P. Yuan, S.X. Chen, Z.T. Xie, L.Y. Xie. (2022). Electrolyte plasma polishing of 316L stainless steel for jewelry. *Electroplating & Finishing,* DOI: 10.19289/j.1004-227x.2023.10.006.

[22] D.K. Liu, X.W. Zong, P.S. Xue, Z.T. Gao, W.J. Wu, Z.Q. Song, F. Ye, Y. Pang, Y. Zhang, H.Z. Zhou, H. Li, B.H. Lu. (2025). Effects of plasma electrolytic polishing treatment on the surface morphology, microstructure and corrosion resistance of additively manufactured TC4 titanium alloy. *Journal of Materials Research and Technology*, DOI: https://doi.org/10.1016/j.jmrt.2025.03.067.

[23] X.C. Ge. (2023). Research on key technologies for high-efficiency and precision electrolytic machining of rifling in thin-walled aluminum alloy tubes. *Master's Thesis, Xi 'an Technological University*, DOI: 10.27391/d.cnki.gxagu.2023.000738.

[24] B.W. Xue, Z.X. Li, D.S. Chang, Y.F. Gao. (2008). Study on Barrel Inner Surface Finishing Method of Rifled Gun. *Journal of Gun Launch & Control,* DOI: 10.19323/j.issn.1673-6524.2008.04.017.

[25] J. Wang, L.C. Suo, L.L. Guan, Y.L. Fu. (2012). Analytical study on mechanism of electrolysis and plasma polishing. *Advanced Materials Research*, DOI: https://doi.org/10.4028/www.scientific.net/AMR.472-475.350.

[26] Y.J. Chen, J. Yi, Z.W. Wang, B. Chen, H. Deng. (2025). Multi-physical field coupling simulation and experimental research on electrolyte plasma polishing. *Journal of Mechanical Engineering,* DOI: 10.3901/JME.2025.01.360.

[27] M.H. Fakhar, A. Fakhar, H. Tabatabaei, H Nouri-Bidgoli. (2020). Investigation of instable fluid velocity in pipes with internal nanofluid flow based on Navier-Stokes equations. *Journal of Computational Applied Mechanics*, DOI:

10.22059/JCAMECH.2020.300244.496.

[28] F. Yang, Z.J. Fan, G.G. Zhao. (2010). The research of the ECM machining gap on tube rifings using COMSOL. *Machinery Design & Manufacture*, DOI: 10.19356/j.cnki.1001-3997.2010.04.051.

[29] Y. Wu, F. Yang, G.G. Zhao, T.Q. Huang, B.X. Liu. (2024). Flow field optimization and process experimentation for electrochemical machining of special-shaped grooves on the inner surface of thin-walled cylinders. *Electromachining & Mould,* DOI: 10.3969/j.issn.1009-279X.2024.z1.007.